



# CHORUS

This is the accepted manuscript made available via CHORUS. The article has been published as:

## Active Nematic Defects and Epithelial Morphogenesis

Farzan Vafa and L. Mahadevan

Phys. Rev. Lett. **129**, 098102 — Published 26 August 2022

DOI: [10.1103/PhysRevLett.129.098102](https://doi.org/10.1103/PhysRevLett.129.098102)

# Active nematic defects and epithelial morphogenesis

Farzan Vafa<sup>1,2</sup> and L. Mahadevan<sup>3,4</sup>

<sup>1</sup>*Department of Physics, University of California Santa Barbara, Santa Barbara, CA 93106, USA*

<sup>2</sup>*Center of Mathematical Sciences and Applications, Harvard University, Cambridge, MA 02138, USA*

<sup>3</sup>*School of Engineering and Applied Sciences, Harvard University, Cambridge, MA 02138, USA*

<sup>4</sup>*Departments of Physics, and Organismic and Evolutionary Biology, Harvard University, Cambridge, MA 02138, USA*

(Dated: July 7, 2022)

Inspired by recent experiments that highlight the role of nematic defects in the morphogenesis of epithelial tissues, we develop a minimal framework to study the dynamics of an active curved surface driven by its nematic texture. Allowing the surface to evolve via relaxational dynamics leads to a theory linking nematic defect dynamics, cellular division rates, and Gaussian curvature. Regions of large positive (negative) curvature and positive (negative) growth are co-localized with the presence of positive (negative) defects. In an ex-vivo setting of cultured murine neural progenitor cells, we show that our framework is consistent with the observed cell accumulation at positive defects and depletion at negative defects. In an in-vivo setting, we show that the defect configuration consisting of a bound  $+1$  defect state, which is stabilized by activity, surrounded by two  $-1/2$  defects can create a stationary ring configuration of tentacles, consistent with observations of a basal marine invertebrate *Hydra*.

Morphogenesis, the development of self-organized form in biology, results from the complex interplay of mechanical and biochemical processes [1–3]. To understand the dynamics of form, we need to complement our knowledge of the molecular constituents that unify many developmental programs with coarse-grained theories that couple flows, forces, and self-regulation to generate shape and link them to testable experimental predictions [4–7]. At the cellular level, there are four geometric fields—cell number, size, shape, and position—that vary in space and time and are responsible for generating shape. In plant tissues, where cells do not change their relative positions, there has been much progress in linking molecular and cellular processes to tissue shaping [8, 9], while in animal tissues, the ability to tag and track thousands of cells in space and time [10–12] allow us to begin answering similar questions linking cellular processes to tissue shape [13–15].

A particularly intriguing question in thin layered epithelial tissues is the role of topological defects in controlling morphogenesis, seen in experimental observations of cell extrusion [16, 17], layer formation [18], and body shaping using bulges, pits and tentacles [19]. Complementing work on the role of defects in passive surfaces that allow the *induced* geometry to relax e.g. [20–22], here we address how topological defects couple to the intrinsic geometry of surfaces ( Fig. 1) via a minimal theory for the relaxational dynamics of the *intrinsic* geometry of active epithelial surfaces (see [23] for a recent review). Our model of epithelial layers is a dynamical theory of active nematics, which consist of head-tail symmetric, elongated units that consume energy to move and do work on their surroundings, while still tending to align, locally generating nematic (apolar) order [24–26]. Like their passive counterparts, active nematics exhibit singular distortions, i.e. topological defects which interrupt the nematic order [27] for a brief overview).

A minimal model that couples the relevant degrees of freedom in an active system must allow for spatio-temporal variations in the two-dimensional nematic tensor  $Q^{ab}$ , an active velocity field  $v^a$  determined by the local nematic field, and

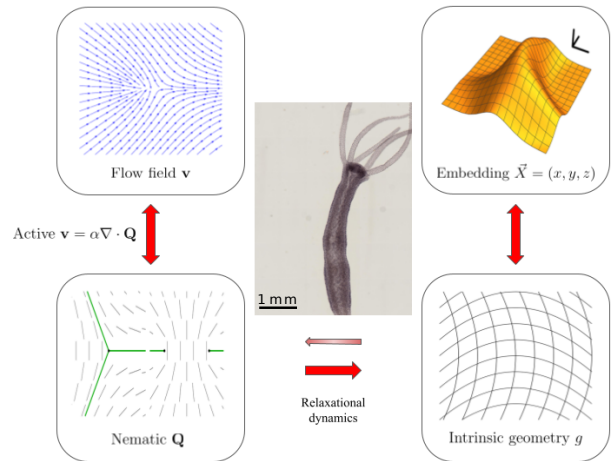


**Figure 1: Schematic of our model.** Epithelial activity driven by a nematic texture leads to a flow field that drives nematic defects. The defects then induce variations in the intrinsic metric and thence changes in the 3-d embedding of the epithelial surface. Image of *Hydra* in the center, adapted from [28].

the geometry of the sheet, characterized by its 2D metric  $g_{ab}$  (which can be deduced from tissue geometry), and its embedding in three dimensions. For simplicity, we will assume that how the surface sits in 3D (the extrinsic geometry) can be deduced entirely by the shape of the 2D surface (the intrinsic geometry), and that the dynamics of the other fields follows a combination of variations in the free energy and active flow dynamics.

The two main contributions to the free energy that we consider are due to: (i) the nematic tensor  $Q^{ab} = A[\hat{n}^a \hat{n}^b - \frac{1}{2} \delta^{ab}]$ , where  $A$  is the magnitude of the nematic order, and  $\hat{n}^\mu$  is the local director field (ii) the metric  $g_{ab}$ . Then the total free energy  $\mathcal{F}$  is the sum of contributions from the nematic field as well as from the intrinsic metric, with  $\mathcal{F} = \mathcal{F}_Q + \mathcal{F}_g$ . Here, the two-dimensional Landau-de Gennes free energy [29],  $\mathcal{F}_Q$ , in its covariant form, is given by

$$\begin{aligned}
\mathcal{F}_Q &= \int d^2x \sqrt{g} [\tilde{K} g_{bd} \nabla_a Q^{ab} \nabla_c Q^{cd} - K' R \text{Tr}[Q^2] \\
&\quad + \frac{1}{4} \epsilon^{-2} (1 - 2g_{bc} g_{ad} Q^{ab} Q^{cd})^2] \\
&= \int d^2x \sqrt{g} [\tilde{K} \text{Tr}[(\nabla \cdot Q)^2] - K' R \text{Tr}[Q^2] \\
&\quad + \frac{1}{4} \epsilon^{-2} (1 - 2 \text{Tr}[Q^2])^2] \quad (1)
\end{aligned}$$

where  $g_{ab}$  is the metric,  $\nabla_\alpha$  is the covariant derivative associated with it, and  $R$  is the scalar curvature. Here  $\tilde{K}$  is the Frank elasticity parameter in the single-constant approximation,  $K' > 0$  is a curvature elasticity that can be viewed as a geometric contribution to the potential: with  $R > 0$  ( $< 0$ ), this term favors ordered (disordered) state, while last term governs the isotropic-nematic transition, with  $\epsilon$  controlling the microscopic nematic correlation length [30]. We further assume that the surface relaxes via relaxational dynamics analogous to diffusion; a naturally invariant form is then given by Ricci flow [31],

$$\partial_t g_{ab} = -DR_{ab} + \lambda g_{ab} \quad (2)$$

where  $R_{ab}$  is the Ricci tensor (which in 2D is given by  $R_{ab} = \frac{1}{2} R g_{ab}$ ),  $D > 0$  is the diffusivity, and  $\lambda(t) > 0$  controls the growth rate of the area. In general,  $\lambda = \lambda(x, t)$ , but for simplicity we will take  $\lambda = \lambda(t)$ . Eq. (2) follows from the gradient-flow of the free energy  $\mathcal{F}_g = \int d^2x \sqrt{g} [K_\varphi R \varphi - \lambda]$  where  $\sqrt{g} = \exp(\varphi)$  [32].  $K_\varphi (\propto D)$  is an elastic constant penalizing changes in the Gaussian curvature  $R$ .

Then the coupled dynamics of the nematic and metric fields associated with gradient descent and advection by a non-equilibrium flow  $v^c$  [33] yields

$$\partial_t Q^{ab} = -v^c \nabla_c Q^{ab} + [Q, \Omega]^{ab} - \gamma_Q^{-1} g^{ac} g^{bd} \frac{1}{\sqrt{g}} \frac{\delta \mathcal{F}}{\delta Q^{cd}} \quad (3)$$

$$\partial_t g_{ab} = -(\nabla_a v^c) g_{cb} - (\nabla_b v^c) g_{ca} - \gamma_\varphi^{-1} \frac{1}{\sqrt{g}} \frac{\delta \mathcal{F}}{\delta g^{ab}}, \quad (4)$$

with  $\Omega_{ab} = (\nabla_a v_b - \nabla_b v_a)/2$  the vorticity, and  $\gamma_Q$  and  $\gamma_\varphi$  are the viscous coefficients for the dynamics of  $Q^{ab}$  and  $g_{ab}$ , respectively, with units of radians<sup>2</sup>/time.

Closure of the system (3)-(4) requires an equation for the active velocity field generated by the active stress  $\sigma^{ab}$ . We note that in Eq. (3) we have ignored the rate of strain alignment; in the biologically relevant, overdamped limit described by Eq. (5) this effect leads to a renormalization of the rigidity constant [34, 35]. In this context,  $\sigma^{ab} = \tilde{\alpha} Q^{ab}$  [24, 36]; i.e. we balance the active stresses with the substrate friction (neglecting elastic and non-local hydrodynamic effects [37]), and therefore write [33]

$$\mu v^c = \tilde{\alpha} \nabla_a Q^{ac}. \quad (5)$$

Here  $\mu$  is the substrate friction,  $\tilde{\alpha}$  is the active energy density with  $\tilde{\alpha} > 0$  ( $\tilde{\alpha} < 0$ ) corresponding to contractile (extensile) activity. We define the scaled activity coefficient  $\alpha = \tilde{\alpha}/\mu$ .

In terms of the problem parameters:  $\tilde{K}$ ,  $K'$ ,  $\epsilon$ ,  $\alpha$ ,  $K_\varphi$ ,  $\gamma_Q$ ,  $\gamma_\varphi$ , and the system size  $L$ , we can define the nematic

coherence length (or defect core radius)  $\xi = \sqrt{\tilde{K}}\epsilon$ , the geometric coherence length  $\ell_\varphi = \sqrt{K_\varphi}\epsilon$ , a ‘‘Gaussian curvature’’ length  $\ell_{R,Q} = \sqrt{K'}\epsilon$ , and  $\ell_d = \sqrt{\tilde{K}/|\tilde{\alpha}|}$ , the defect separation length [38]; and the relaxation times  $\tau_Q = \gamma_Q \epsilon^2$  and  $\tau_\varphi = \gamma_\varphi L^2 / K_\varphi$ . This leads to the following dimensionless quantities:  $\xi/\ell_\varphi$ , the ratio of coherence lengths for the nematic field and intrinsic geometry ( $< 1$  because extrinsic geometry variations occur on scales large compared to the nematic defect core size);  $\tau_\varphi/\tau_Q = (\gamma_\varphi/\gamma_Q)(L/\ell_\varphi)^2$  ( $\gg 1$  because we assume that the long wavelength extrinsic geometry relaxes slowly compared to the local nematic order); and  $K/K' \sim 1$ , where  $K = \tilde{K} - K'$ , which as we will discuss later is the ratio of the two different types of nematic elastic deformations. See the Supplemental Material [27] for estimates of model parameters.

Eqs. (3) to (5) form a set of nonlinear partial differential equations that dictate the evolution of the nematic field  $Q^{ab}$  and the intrinsic geometry  $g_{ab}$  as a function of the activity  $\alpha$ , when complemented by appropriate initial and boundary conditions. To make progress in a minimal setting for epithelial morphogenesis, we choose 2D isothermal (conformal) [39] complex coordinates  $z$  and  $\bar{z}$  such that

$$ds^2 = g_{z\bar{z}} dz d\bar{z} + g_{\bar{z}z} d\bar{z} dz = 2g_{z\bar{z}} |dz|^2 = e^\varphi |dz|^2 \quad (6)$$

and assume that the metric remains diagonal in these coordinates for all time. Furthermore, since the nematic tensor  $Q^{ab}$  is a traceless real bivector, we can write its components  $Q = Q^{zz}$ ,  $\bar{Q} = Q^{\bar{z}\bar{z}}$ , and  $Q^{z\bar{z}}$ , with  $Q^{z\bar{z}} = 0$ , and  $Q = (\bar{Q})^*$ . Since the metric  $g_{z\bar{z}}$  measures the area in the  $z$  coordinate system, assuming fixed cell size, this implies that we can interpret  $\varphi = \log g_{z\bar{z}}$ , i.e. the log of the cell density in these coordinates. In particular, the change in  $\varphi$  reflects cell division. In these coordinates,  $\mathcal{F}_Q$  takes the form

$$\begin{aligned}
\mathcal{F}_Q &= \int d^2z \sqrt{g} [2K g_{z\bar{z}} \nabla_z Q^{zz} \nabla_{\bar{z}} Q^{\bar{z}\bar{z}} + 2K' g_{z\bar{z}} \nabla_{\bar{z}} Q^{z\bar{z}} \nabla_z Q^{z\bar{z}} \\
&\quad + \frac{1}{4} \epsilon^{-2} (1 - 4g_{z\bar{z}} g_{z\bar{z}} Q^{zz} Q^{\bar{z}\bar{z}})^2] \\
&= \int d^2z \sqrt{g} [2K |\nabla_z Q|^2 + 2K' |\nabla_{\bar{z}} Q|^2 + \frac{1}{4} \epsilon^{-2} (1 - 4|Q|^2)^2] \quad (7)
\end{aligned}$$

where  $K = \tilde{K} - K' > 0$  to guarantee positivity of the elastic energy,  $Q = Q^{zz}$  and  $\bar{Q} = Q^{\bar{z}\bar{z}}$ , and  $|\cdot|$  is defined in terms of the metric [40]. Here the covariant derivatives  $\nabla_z Q^{zz} = \partial Q + 2(\partial\varphi)Q$  and  $\nabla_{\bar{z}} Q^{z\bar{z}} = \bar{\partial}Q$ , while the scalar curvature  $R = -4e^{-\varphi} \partial\bar{\partial}\varphi$ . The asymmetry in the appearance of  $\partial\varphi$  in  $\nabla_z Q$  and  $\nabla_{\bar{z}}$  is the underlying reason behind asymmetry in cell growth near defects: cells accumulate at positive defects and deplete at negative defects.

As a preliminary step before considering active defects, we consider the case of passive nematics with  $\alpha = 0$ . Then the dynamics for  $Q$  and  $\varphi$  in isothermal conformal coordinates can be written as

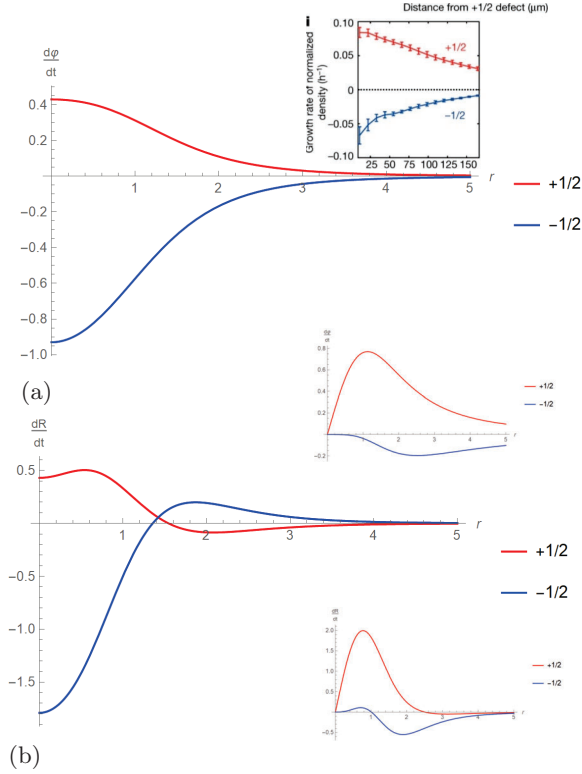


Figure 2: **Dynamics near defects.** Following Eqs. (10) and (11), where  $R = -4e^{-\varphi}\partial\bar{\partial}\varphi$ , we show plots of (a)  $\frac{d\varphi}{dt}$  and (b)  $\frac{dR}{dt}$  for a single +1/2 (in red) and a single -1/2 defect (in blue), with the activity  $\alpha = 0$ . Top inset: for comparison, we show the experimental growth rate of normalized cell density [17]. Middle and bottom insets: corresponding plots of active contribution for  $\frac{d\varphi}{dt}$  and  $\frac{dR}{dt}$  for  $\phi = 0, \alpha = 1$ . Parameters used are  $K = 1, K' = 1, \epsilon = 1$ .

$$\gamma_Q \partial_t Q = 2K g^{z\bar{z}} \nabla_{\bar{z}} \nabla_z Q + 2K' g^{z\bar{z}} \nabla_z \nabla_{\bar{z}} Q + 2\epsilon^{-2}(1 - 4|Q|^2)Q \quad (8)$$

$$\gamma_\varphi \partial_t \varphi = -K_\varphi R + 4K |\nabla_z Q|^2 + 4K g_{z\bar{z}} (Q \nabla_z \nabla_{\bar{z}} \bar{Q} + \bar{Q} \nabla_{\bar{z}} \nabla_z Q) - 4K' |\nabla_{\bar{z}} Q|^2 - \frac{1}{4}\epsilon^{-2}(1 - 4|Q|^2)(1 - 20|Q|^2) + \lambda, \quad (9)$$

146 where the covariant derivative terms are  $\nabla_{\bar{z}} \nabla_z Q = \bar{\partial}\partial Q +$   
147  $2(\bar{\partial}\partial\varphi)Q + 2\partial\varphi\bar{\partial}Q$  and  $\nabla_z \nabla_{\bar{z}} Q = \partial\bar{\partial}Q + 2\partial\varphi\bar{\partial}Q$ .

148 For a flat configuration with  $\varphi = 0$ , denoting  $\varphi^\pm$  and  $Q^\pm$   
149 as the local geometry and nematic field in the neighborhood  
150 of  $\pm 1/2$  defects, Eq. (9) in the neighborhood of a defect  
151 simplifies to

$$\begin{aligned} \gamma_\varphi \partial_t \varphi^+ &= 4K |\partial Q^+|^2 + 2K(Q^+ \partial \bar{\partial} \bar{Q}^+ + \bar{Q}^+ \bar{\partial} \partial Q^+) \\ &\quad - 4K' |\bar{\partial} Q^+|^2 - \frac{1}{4}\epsilon^{-2}(1 - 4|Q^+|^2)(1 - 20|Q^+|^2) + \lambda \end{aligned} \quad (10)$$

$$\begin{aligned} \gamma_\varphi \partial_t \varphi^- &= 4K |\partial Q^-|^2 + 2K(Q^- \partial \bar{\partial} \bar{Q}^- + \bar{Q}^- \bar{\partial} \partial Q^-) \\ &\quad - 4K' |\bar{\partial} Q^-|^2 - \frac{1}{4}\epsilon^{-2}(1 - 4|Q^-|^2)(1 - 20|Q^-|^2) + \lambda \end{aligned} \quad (11)$$

152 Now noting that  $Q^+ = (Q^-)^*$  and that in the vicinity of  
153 the positive (negative) defect core  $\bar{\partial}Q^+ (\partial Q^-) = 0$  leads to

$$\begin{aligned} \gamma_\varphi \partial_t \varphi^+ - \gamma_\varphi \partial_t \varphi^- &= 4K |\partial Q^+|^2 + 4K' |\bar{\partial} Q^-|^2 \\ &= 4\tilde{K} |\partial Q^+|^2 > 0. \end{aligned} \quad (12)$$

154 Interpreting  $\varphi$  as the logarithm of the cell density (since  
155 the Gaussian curvature  $R = -4e^{-\varphi}\partial\bar{\partial}\varphi$ ), in the absence  
156 of net surface growth, this implies that  $\varphi$  will increase at  
157 a +1/2 defect and decrease near a -1/2 defect (since the  
158 two changes must balance each other), and the cell density  
159 will increase (decrease) at plus (minus) defects, i.e. cells  
160 accumulate (deplete) at the defects. This shows that in a  
161 passive setting without activity, positive curvature growth  
162 via a positive defect can still occur. The mechanism we  
163 propose is a geometric alternative to previously-proposed  
164 mechanisms for cell accumulation at topological defects due  
165 to anisotropic friction [17, 18], and can operate either in-  
166 dependently or together with previously-proposed mecha-  
167 nisms.

168 In the top panel of Fig. 2, we show the initial profile of  
169  $\varphi$  at  $t = 0$  from our analysis, showing the dynamic asym-  
170 metry between a plus and minus defect, consistent with the  
171 experimental observations of cell density in the vicinity of  
172 defects in murine neural progenitor epithelia [17]. In the  
173 bottom panel of Fig. 2, we show that this asymmetry in  
174 the shape in the neighborhood of  $\pm 1/2$  defects is reflected  
175 in the Gaussian curvature of the surface which is positive  
176 (negative) near a plus (minus) defect, consistent with inde-  
177 pendent observations in a different experiment [19].

178 Activity, i.e.  $\alpha \neq 0$ , leads to anisotropic flow because  
179 of gradients in the nematic order parameter; this acts as  
180 an additional source of geometric frustration, modifying the  
181 Gaussian curvature of the sheet [27]. More generally, we  
182 rewrite the coupled Eqs. (8) and (9) in complex coordinates  
183 with  $\partial_t Q \rightarrow D_t Q = \partial_t Q + v^z \nabla_z Q + v^{\bar{z}} \nabla_{\bar{z}} Q - (\nabla_z v^z -$   
184  $\nabla_{\bar{z}} v^{\bar{z}})Q$  and  $\partial_t \varphi \rightarrow D_t \varphi = \partial_t \varphi + 2(\nabla_z v^z + \nabla_{\bar{z}} v^{\bar{z}})$ , where  
185 in the over-damped limit,  $v^z = \alpha \nabla_z Q = \alpha[\partial Q + 2(\partial\varphi)Q]$   
186 and  $\nabla_z v^z = \partial_z v^z + (\partial\varphi)v^z$ . To solve these equations and  
187 follow the nematic field and the intrinsic geometry, we use a  
188 finite-difference scheme with periodic boundary conditions  
189 to simulate a ring-like structure seen in *Hydra* [27].

190 We find that an initially flat geometry with a single +1  
191 defect in the center and two -1/2 defects on the edges, using  
192 the ansatz from [41], settles into a stationary defect config-  
193 uration of a ring of equally spaced +1 defects (bound state  
194 of two +1/2 defects) separated by pairs of -1/2 defects in a  
195 cylindrical geometry (see Fig. 3(a)), similar to that observed

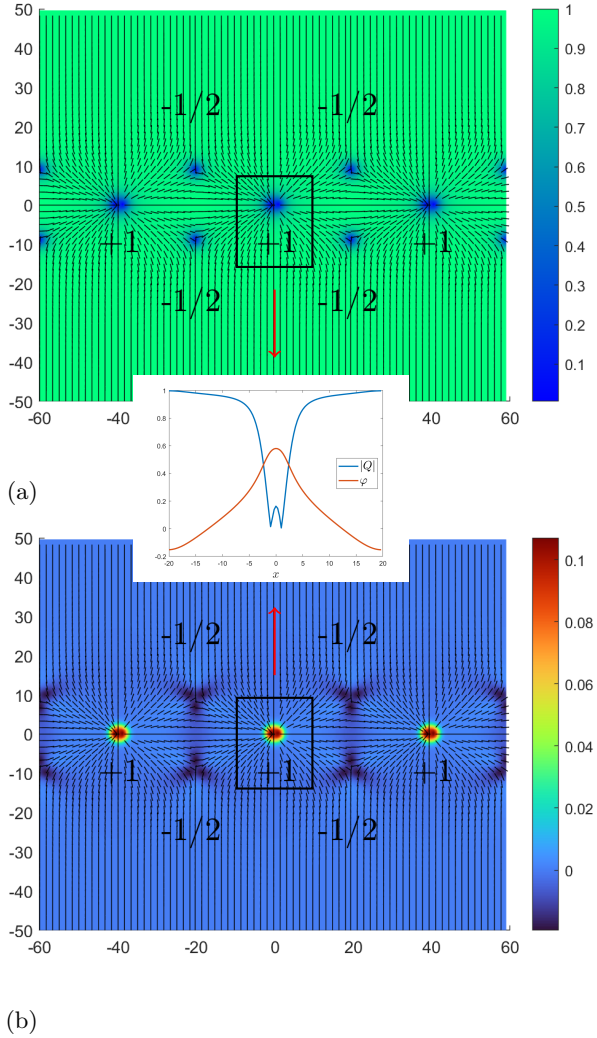


Figure 3: **Defect texture and geometry.** We numerically integrate Eqs. (8) and (9) (with the substitution  $\partial_t \rightarrow D_t$ ) to obtain steady state plots of (a) the magnitude of the nematic order parameter  $|Q|$  and (b) the curvature density (given by  $-4\partial\bar{\partial}\varphi$ ). We note that the sign of the curvature correlates with the sign of the defect, and that the defect configuration is a lattice of  $+1$  bound states separated by pairs of  $-1/2$  defects. In the inset, we show the profile of the nematic order  $|Q|$  (blue) and  $\varphi$  (red) along the  $x$ -axis. The profile of  $|Q|$ , which is dictated by the nematic coherence length, is smaller than the width of the profile of  $\varphi$  since  $\ell_\varphi > \xi$ . Parameters for simulations:  $\alpha = -0.8$ ,  $K = 1$ ,  $K' = 0$ ,  $\gamma_Q = \gamma_\varphi = 1$ ,  $K_\varphi = 4$ , and  $\epsilon = 2$ , in terms of which  $\xi = 1$ ,  $\ell_{R,Q} = 1$ , and  $\ell_\varphi = 2$ . See text and the Supplemental Material [27] for details.

in [19]. Activity plays a key role in stabilizing this configuration, and in particular, the  $+1$  bound state is a result of balance of Coulombic repulsion between the defects and active motility [27]. Indeed, the larger the activity parameter for the extensile case  $\alpha < 0$ , the tighter is the  $+1$  bound defect. Moreover, the curvature is positive near a plus defect, and negative near a minus defect, as can be seen in Fig. 3(b).

Plotting the profiles of  $|Q|$  and  $\varphi$  along the vertical  $x$ -axis, we find that the peak in  $\varphi$  near the origin indicates outward bulging of the geometry. Moreover, the profile of  $|Q|$  which is dictated by the nematic coherence length is much narrower than the width of  $\varphi$  along the  $x$ -axis, which is expected given that the geometric coherence length is larger than the nematic coherence length, i.e.  $\ell_\varphi > \xi$  and similar to what was observed experimentally in [17] and in numerical simulations of phase field models e.g. [42]. (See [27] for a plot of the flow field at a late time).

To ground these results, we turn to observations of epithelial morphogenesis in *Hydra*, a small, fresh-water basal marine invertebrate that has been a model organism for studying the dynamics of body shaping [19, 43, 44]. The tubular body of the organism consists of a bilayer of epithelial cells which contains condensed supracellular actin fibers which align parallel to the body axis in the outer (ectoderm) layer and perpendicular to the body axis in the inner (endoderm) layer [45]. A variable number of tentacles form a ring around the body, near the head, and form when a single  $+1$  defect is surrounded by a pair of  $-1/2$  defects [19], with the sign of the curvature is correlated with the sign of the defect, consistent with our results summarized in Fig. 3. Indeed, a qualitative rendering of the shape associated with the presence of these bound defect states shown in Fig. 4(a) provides a simple projective view of the body plan in the neighborhood of the ring of tentacles.

Although knowing the intrinsic geometry does not always allow us to deduce the extrinsic geometry, it is possible to get a numerical approximation (see SI-Algorithm for finding embedding) of the local shape of the active surface as shown in Fig. 4(b),(c) near a  $+1$  defect. Furthermore, we see that at early times the time evolution of the height follows the scaling law  $h \propto \sqrt{t}$ , which can be analytically derived by using Eq. (10) (see SI-Algorithm for finding embedding).

Our minimal framework coupling the dynamics of an active nematic field on a curved surface to the intrinsic geometry of the surface via relaxational dynamics has focused on the interplay between geometry and nematic defects and leads to three simple conclusions: (i) the sign of the curvature is correlated with the sign of the defect, (ii) cells accumulate and form mounds at positive defects and are depleted at negative defects, and (iii) a stationary ring configuration of equally spaced  $+1$  defects separated by pairs of  $-1/2$  defects can form. These results are consistent with experimental observations in different systems such as neural progenitor cells in-vitro and *Hydra* morphogenesis in-vivo. Moving forward, a more complete description must include a complete characterization of the dynamics of embedding and the possible time-dependence of isothermal coordinates, e.g. using phase field models for active deformable shells [42, 46] that account for both the induced and the intrinsic geometry of the manifolds, but now including feedback on activity of the form  $\alpha = \alpha(Q^{ab}, g_{ab}, \dots)$ , potential directions for future work. Indeed, a recent preprint [47] submitted after the first version of the current paper was submitted has begun to address some closely-related questions.

We thank Xianfeng David Gu and Shing-Tung Yau for valuable discussions on reconstructing the embedding from

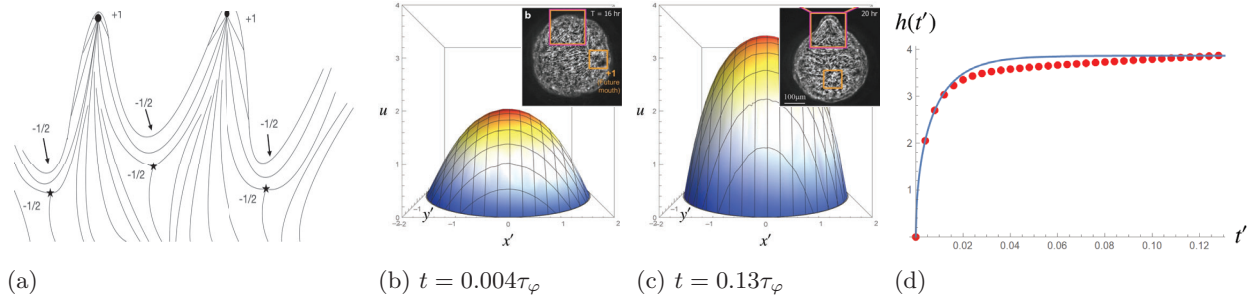


Figure 4: **Extrinsic geometry.** In (a), sketch of the geometry for the tentacle configuration from our simulation. The black dots represent  $+1$  defects, the stars represent  $-1/2$  defects, and black lines depict the nematic order. Three of the  $-1/2$  defects are on the opposite side. In (b) and (c): snapshots from simulations of height  $u$  of tentacle in real space near a  $+1$  defect for early and late times, where insets (adapted from [19]) are snapshots of tentacle formation near a  $+1$  defect for early and late times. In (d), plot of the height  $h(t)$  at the center of the  $+1$  defect as a function of time  $t$ . Red points are data from simulation and blue curve is the fit  $h(t) = h_0[1 - \exp(-t/\tau)]^{1/2}$ , where we find that  $h_0 = 3.87L$  and  $\tau = 0.01\tau_\varphi$ . Initially,  $h(t) \propto \frac{L}{\xi} \frac{L}{\ell_\varphi} L \sqrt{\frac{t}{\tau_\varphi}}$  and  $\tau \propto \tau_\varphi$ . See the Supplemental Material [27] for details. All plots use rescaled coordinates  $x' = x/L$ ,  $y' = y/L$ , and  $t' = t/\tau_\varphi$ .

- 262 the intrinsic metric, and discussions with Suraj Shankar, 297  
 263 and Cristina Marchetti and Mark Bowick groups at UCSB. 298  
 264 This work is partially supported by the Center for Math- 299  
 265 ematical Sciences and Applications at Harvard University 300  
 266 (F. V.) and the NSF Simons Center for Mathematical and 301  
 267 Statistical Analysis of Biology Award No. 1764269 (L. M.). 302
- 
- 268 [1] D. W. Thompson, *On Growth and Form* (Cambridge Univ. 297  
 269 Press, 1917). 298  
 270 [2] M. J. F. Barresi and S. F. Gilbert, *Developmental biology*, 299  
 271 12th ed. (Sinauer Associates, 2020). 300  
 272 [3] T. Lecuit and L. Mahadevan, *Development* **144**, 4197 301  
 273 (2017). 302  
 274 [4] C.-P. Heisenberg and Y. Bellaïche, *Cell* **153**, 948 (2013). 303  
 275 [5] P. Gross, K. V. Kumar, and S. W. Grill, *Annual Review of* 304  
 276 *Biophysics* **46**, 337 (2017), pMID: 28532214. 305  
 277 [6] L. Mahadevan, Proc. 27th Solvay conference on physics: 306  
 278 physics of living matter, ed. D. Gross, B. Shraiman (World 307  
 279 Scientific, 2020). 308  
 280 [7] C. Collinet and T. Lecuit, *Nature Reviews Molecular Cell* 309  
 281 *Biology* **22**, 245 (2021). 310  
 282 [8] E. M. Meyerowitz, *Cell* **88**, 299 (1997). 311  
 283 [9] E. Coen, R. Kennaway, and C. Whitewoods, *Development* 312  
 284 **144**, 4203 (2017). 313  
 285 [10] F. Bosveld, I. Bonnet, B. Guirao, S. Tlili, Z. Wang, A. Peti- 314  
 286 talot, R. Marchand, P.-L. Bardet, P. Marcq, F. Graner, and 315  
 287 Y. Bellaïche, *Science* **336**, 724 (2012). 316  
 288 [11] R. Tomer, K. Khairy, F. Amat, and P. J. Keller, *Nature* 317  
 289 *Methods* **9**, 755 (2012). 318  
 290 [12] U. Krzic, S. Gunther, T. E. Saunders, S. J. Streichan, and 319  
 291 L. Hufnagel, *Nature Methods* **9**, 730 (2012). 320  
 292 [13] R. Farhadifar, J.-C. Röper, B. Aigouy, S. Eaton, and 321  
 293 F. Jülicher, *Current Biology* **17**, 2095 (2007). 322  
 294 [14] N. C. Heer and A. C. Martin, *Development* **144**, 4249 323  
 295 (2017). 324  
 296 [15] K. D. Irvine and B. I. Shraiman, *Development* **144**, 4238 325  
 (2017). 326  
 [16] T. B. Saw, A. Doostmohammadi, V. Nier, L. Kocgozlu, 327  
 S. Thampi, Y. Toyama, P. Marcq, C. T. Lim, J. M. Yeomans, 328  
 and B. Ladoux, *Nature* **544**, 212 (2017). 329  
 [17] K. Kawaguchi, R. Kageyama, and M. Sano, *Nature* **545**, 330  
 327 (2017). 331  
 [18] K. Copenhagen, R. Alert, N. S. Wingreen, and J. W. Shaevitz, 332  
*Nature Physics* **17**, 211 (2021). 333  
 [19] Y. Maroudas-Sacks, L. Garion, L. Shani-Zerbib, A. Livshits, 334  
 E. Braun, and K. Keren, *Nature Physics* (2020), 335  
 10.1038/s41567-020-01083-1. 336  
 [20] T. C. Lubensky and J. Prost, *Journal de Physique II* **2**, 371  
 (1992).  
 [21] H. S. Seung and D. R. Nelson, *Phys. Rev. A* **38**, 1005 (1988).  
 [22] J. R. Frank and M. Kardar, *Phys. Rev. E* **77**, 041705 (2008).  
 [23] S. C. Al-Izzi and R. G. Morris, *Seminars in Cell & Developmental Biology* **120**, 44 (2021), special issue: The mechanics of development by Timothy Saunders and Ivo Telley.  
 [24] M. C. Marchetti, J.-F. Joanny, S. Ramaswamy, T. B. Liverpool, J. Prost, M. Rao, and R. A. Simha, *Reviews of Modern Physics* **85**, 1143 (2013).  
 [25] A. Doostmohammadi, J. Ignés-Mullol, J. M. Yeomans, and F. Sagués, *Nature communications* **9**, 3246 (2018).  
 [26] S. Shankar, A. Souslov, M. J. Bowick, M. C. Marchetti, and V. Vitelli, “Topological active matter,” (2020), arXiv:2010.00364 [cond-mat.soft].  
 [27] See Supplemental Material at [URL] for further details on topological defects, Ricci flow, model parameters, role of activity, numerical simulations, and dynamics of bud growth, which additionally includes Refs. [48–60].  
 [28] D. J. Drew, “Hydra (YPM IZ 091796),” Digital Image: Yale Peabody Museum of Natural History (2018).  
 [29] P. G. de Gennes and J. Prost, *The physics of liquid crystals* (Clarendon Press, Oxford, 1993).  
 [30] Unlike in situations where the metric remains fixed, as in the elastomeric case [61], here we allow it to vary dynamically, so that the liquid crystalline flows can generate curvature via defects. Moreover, in Ref. [61], positive defects generate negative curvature, contrary to both recent experiments [17, 19] and our model and simulations.

- [31] R. S. Hamilton, *J. Differential Geom.* **17**, 255 (1982).
- [32] This is a manifestation of the well-known trace anomaly, where the response of the system to conformal rescaling of the metric is proportional to the curvature  $R$  [62].
- [33] A. N. Beris and B. J. Edwards, *Thermodynamics of flowing systems: with internal microstructure* (Oxford Univ. Press, 1994).
- [34] P. Srivastava, P. Mishra, and M. C. Marchetti, *Soft Matter* **12**, 8214 (2016).
- [35] E. Putzig, G. S. Redner, A. Baskaran, and A. Baskaran, *Soft Matter* **12**, 3854 (2016).
- [36] R. Aditi Simha and S. Ramaswamy, *Phys. Rev. Lett.* **89**, 058101 (2002).
- [37] In the limit that  $K/(\alpha\mu L^2), \gamma/(\mu L^2) \ll 1$ , where  $\gamma$  is the viscosity coefficient, we can neglect the elastic stress  $\sigma_{el}^{ab} \sim [Q, \frac{\delta \mathcal{F}}{\delta Q}]^{ab}$  and viscous stress  $\sigma_{vis}^{ab} \sim \gamma(\nabla^a v^b + \nabla^b v^a)$ , so that the active stresses are balanced by the local substrate friction.
- [38] E. J. Hemingway, P. Mishra, M. C. Marchetti, and S. M. Fielding, *Soft Matter* **12**, 7943 (2016).
- [39] F. David, in *Statistical Mechanics of Membranes and Surfaces*, edited by D. Nelson, T. Piran, and S. Weinberg (World Scientific, 2004) 2nd ed., Chap. 7, pp. 149–209.
- [40] In deriving this equation, we used the fact that up to a total derivative,  $R \text{Tr}[Q^2] = 2(|\nabla_z Q|^2 - |\nabla_{\bar{z}} Q|^2)$ .
- [41] F. Vafa, M. J. Bowick, M. C. Marchetti, and B. I. Shraiman, “Multi-defect dynamics in active nematics,” (2020), arXiv:2007.02947 [cond-mat.soft].
- [42] L. Metselaar, J. M. Yeomans, and A. Doostmohammadi, *Physical review letters* **123**, 208001 (2019).
- [43] B. Galliot, *The International Journal of Developmental Biology* **56**, 411–423 (2012).
- [44] E. Braun and K. Keren, *BioEssays* **40**, 1700204 (2018).
- [45] R. Aufschnaiter, R. Wedlich-Söldner, X. Zhang, and B. Hobmayer, *Biology Open* **6**, 1137 (2017).
- [46] A. Mietke, F. Jülicher, and I. F. Sbalzarini, *Proceedings of the National Academy of Sciences* **116**, 29 (2019).
- [47] L. A. Hoffmann, L. N. Carenza, J. Eckert, and L. Giomi, “Defect-mediated morphogenesis,” (2021), arXiv:2105.15200 [cond-mat.soft].
- [48] V. Narayan, S. Ramaswamy, and N. Menon, *Science* **317**, 105 (2007).
- [49] T. Sanchez, D. T. Chen, S. J. DeCamp, M. Heymann, and Z. Dogic, *Nature* **491**, 431 (2012).
- [50] L. Giomi, M. J. Bowick, X. Ma, and M. C. Marchetti, *Physical review letters* **110**, 228101 (2013).
- [51] L. Pismen, *Physical Review E* **88**, 050502 (2013).
- [52] S. Shankar, S. Ramaswamy, M. C. Marchetti, and M. J. Bowick, *Physical review letters* **121**, 108002 (2018).
- [53] K. Thijssen and A. Doostmohammadi, *Phys. Rev. Research* **2**, 042008 (2020).
- [54] F. Vafa, “Defect dynamics in active polar fluids vs. active nematics,” (2020), arXiv:2009.10723 [cond-mat.soft].
- [55] C. F. Gauss, in *A Source Book in Mathematics*, edited by D. E. Smith (Dover, 1959) p. 463–475.
- [56] G. Perelman, “The entropy formula for the ricci flow and its geometric applications,” (2002), arXiv:math/0211159 [math.DG].
- [57] N. Kumar, R. Zhang, J. J. de Pablo, and M. L. Gardel, *Sci. Adv.* **4** (2018).
- [58] Benamou, Jean-David, Froese, Brittany D., and Oberman, Adam M., *ESAIM: M2AN* **44**, 737 (2010).
- [59] X. Gu, F. Luo, J. Sun, and S. T. Yau, “Variational principles for minkowski type problems, discrete optimal transport, and discrete monge-ampere equations,” (2013), arXiv:1302.5472 [math.GT].
- [60] L. Cui, X. Qi, C. Wen, N. Lei, X. Li, M. Zhang, and X. Gu, *Computer-Aided Design* **115**, 181 (2019).
- [61] D. Duffy and J. S. Biggins, *Soft Matter* **16**, 10935–10945 (2020).
- [62] A. Polyakov, *Physics Letters B* **103**, 207 (1981).